Modeling, Analyzing, and Suppression of EMI Effects in Eddy Current Sensors of Active Magnetic Bearings

Yuanhao Xie, *Graduate Student Member, IEEE*, Dong Jiang, *Senior Member, IEEE*,
Jianfu Ding, *Graduate Student Member, IEEE*, and Zicheng Liu, *Senior Member, IEEE*

***Abstract*—The displacement sensor is of vital importance for the levitation control of the active magnetic bearing (AMB). For the most widely used eddy current sensor (ECS), it is easy to be affected by electromagnetic interference (EMI) produced by the high-frequency switching of the AMB drive converter. This phenomenon has been sophisticatedly researched in this article. The circuit model of the ECS along with its conditioning circuits have been constructed to predict the conducted EMI in the sensor up to 30 MHz. The mechanism of the EMI on sensor signals have been analyzed. The impact of high-frequency EMI on low-frequency closed-loop control has also been explained. The suppression methods of the EMI effect on the ECS have been proposed based on either high-frequency or low-frequency mechanism. The experiment results have shown that the constructed model can well predict the effect of EMI in the ECS, and the proposed suppression method can significantly improve the measurement accuracy of the ECS.**

***Index Terms*—Active magnetic bearing, eddy current sensor, electromagnetic interference.**

I. Introduction

THE displacement sensor is an indispensable component in electromechanical systems to achieve accurate position control. As a typical type of noncontact displacement sensor, the eddy current sensor (ECS) is based on the principle of electromagnetic induction, making it insensitive to any nonconductive media. It offers advantages like a simple structure, high sensitivity, and wide frequency response, allowing it to achieve micron-level resolution [1]. As a result, it is widely used in applications such as measuring rotational speed, metal workpiece geometric dimensions, and surface roughness. It is also the most commonly used type of displacement sensor in active magnetic bearings (AMB) [2].

The typical AMB system with ECS is shown in Fig. 1. The AMB is a special type of bearing, which uses the power electronic converter to actively control the electromagnetic force, thus, to achieve stable levitation and position control of rotors. It has advantages such as no friction loss, no lubrication requirements, low noise, and so on, making it a better choice for levitation of high-speed rotating machinery. Also, the AMB is an open-loop unstable system [3], thus, the precise measurement of displacement is of vital importance for its reliable operation.

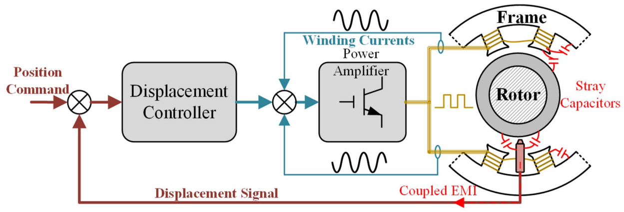

Fig. 1. Working principle of the AMB.

There has been plenty of literatures that concentrate on the optimization of ECSs [4], [5], [6], including selecting the best excitation frequency and geometry [4], improving the efficiency of the drive circuits [5], and increasing the linear degree [6]. More importantly, the working environment of the ECS will also significantly influence its performance. In this regard, plenty of literatures have concentrated on the impact of temperature on ECSs, providing a series of temperature compensation schemes, thus greatly expand the working temperature range [7], [8]. However, the electromagnetic environment will also affect the normal operation of ECSs. When the ECS is applied to AMBs, which is a typical type of electromechanical system, the continuous high-frequency switching actions of power electronic converters can cause electromagnetic interference (EMI) over a wide frequency range. The common mode (CM) EMI has been found easily coupled to the ECS and would cause significant fluctuation on the displacement signal, thus, deteriorate the levitation accuracy [9]. Regarding this issue, there have been some pioneers focusing on the phenomenon of high-frequency interference of sensors in electromechanical systems driven by power converters.

With respect to the analysis method of EMI effect on sensors, a general technique is to conduct the electromagnetic sensitivity tests of the sensors. With this method, the sensor is regarded as a black box. Aiello et al. [10] assessed the Hall effect sensor's susceptibility to EMI using the bulk current injection method, and Lei et al. [11], [12] done the test for the ECS under

Received 8 October 2024; revised 23 December 2024; accepted 19 January 2025. Date of publication 27 January 2025; date of current version 20 March 2025. This work was supported in part by the National Natural Science Foundation of China (NSFC) under Grant 52477189. Recommended for publication by Associate Editor M. Hartmann. *(Corresponding author: Dong Jiang.)*

The authors are with the State Key Laboratory of Advanced Electromagnetic Engineering and Technology, School of Electrical and Electronic Engineering, Huazhong University of Science and Technology, Wuhan 430074, China (e-mail: xieyh@hust.edu.cn; jiangd@hust.edu.cn; djf@hust.edu.cn; liuzc@hust.edu.cn).

Color versions of one or more figures in this article are available at https://doi.org/10.1109/TPEL.2025.3534801.

Digital Object Identifier 10.1109/TPEL.2025.3534801

different kind of EMI. To conduct the tests, the RF generator, power amplifier, and the antenna are needed, so that the sensor can be tested under different type of interference (electric or magnetic field), with different configurations and parameters, thereby achieving repeated optimization and testing process of the sensor. To understand the propagation mechanism of the EMI, the basic approach is to qualitatively analyze the characteristics of the noise source and the coupling path [13], [14]. For quantitative analysis, some researchers have modeled the key components in sensors, which are typically active components. Fiori and Crovetti [15] built nonlinear demodulation models for the interference introduced at the input stage of the operational amplifier (Op-Amp), based on which the high-frequency model of the Op-Amp was constructed with bandwidth above GHz [16]. Sui et al. [17] proposed transfer impedance measurement based model of the power delivery circuit. Furthermore, in the system level, Chen et al. [18] analyzed the CM conducted EMI in variable reluctance resolvers used in the electric vehicles and constructed a behavioral model to predict the interference. Still, the existing researches have seldom provided a sophisticated analysis on the mechanism of EMI affecting ECSs. The analysis of EMI coupling path, as well as the high frequency models of the probe along with the conditioning circuits of the ECS are still to be studied.

With respect to the solution of the EMI effects in sensors, additional passive filters are usually needed in the sensing path [18], [19]. Shielding can be also effective in some certain situations. Yoo et al. [13] built electric field shield for Hall effect current sensor, while Kim et al. [14] built magnetic field shield for motor resolver. Most of these solutions are based on empirical design and lack the guidance of modeling. Another solution is to modify the structure of the sensor, thus, to improve the conduction path of the EMI. Aiello and Fiori [20] and [21] reconstructed integrated current sensors based on Miller effect or Hall effect, thus, to disconnect the original conduction path of EMI. But these works only take the input current wire as single interference source and did not take into account the complex coupling path of EMI in practical application scenarios. Also, since the ECS has a fixed frequency excitation signal, Pan et al. [22] and Nabavi and Nihtianov [23] adopted filters to this signal to reduce the sensitivity of ECS to external interference, but this would be inadequate in dealing with wideband EMI noise caused by power electronic converters.

Furthermore, as the demand for dynamic performance and carrying capability of AMB increases [24], the switching frequency and voltage level of their power electronic converters are also increasing [25], resulting in more severe EMI. Therefore, the electromagnetic compatibility (EMC) of ECSs should be given greater consideration.

In view of these problems, this article aims to quantitatively analyze the impact of EMI from the controller of AMB on the ECSs and tries to propose solutions. The rest of this article is organized as follows. In order to achieve the goals, the basic operation principle of the ECS as well as the analysis of EMI coupling path have been presented in Section II. The high-frequency equivalent circuit model of the ECS along with its conditioning circuit were constructed in Section III, whose accuracy is verified in Section IV. Then, the mechanism of CM EMI on sensor signals were analyzed in Section V. Next, two novel methods right corresponding to the mechanism were proposed in Section VI to significantly suppress the EMI effects in sensor signals, thus, improve the EMC of the ECS. Finally, Section VII concludes this article.

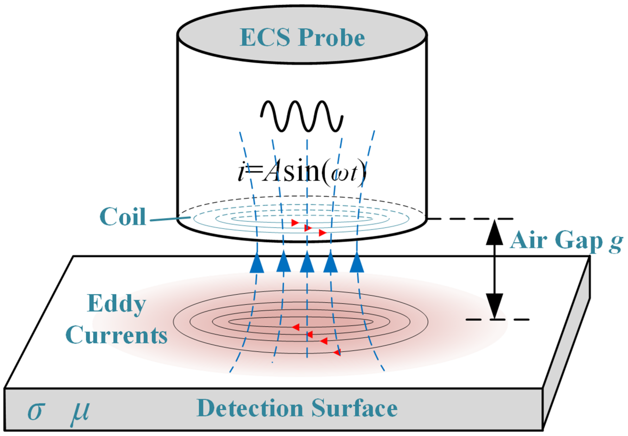

Fig. 2. Schematic diagram of eddy current effect.

II. OPERATION PRINCIPLE AND SYSTEM STRUCTURE OF THE ECS

A. Working Principle of ECSs

The operation principle of the ECS is based on the eddy current effect, as illustrated in Fig. 2. The excitation current on the probe coil will generate a high-frequency varying magnetic field in the air gap between the probe and the detection target, which can induce eddy currents on the detection surface. According to Lenz's law, these eddy currents will weaken the magnetic field in the space, thereby reducing the equivalent inductance of the probe coil. Also, the extra loss caused by eddy current will increase the equivalent resistance of the coil. The impedance of the ECS probe can be presented by

$$Z_{\text{ECS}} = f(g, \rho, \mu, f) \tag{1}$$

where g is the distance between the probe and detection surface, f is the frequency of the excitation current, which is set as constant, ρ and μ are the conductivity and permeability of the detection surface, respectively, both of which are constant values. Therefore, only the distance g will influence the coil impedance, the displacement measurement can be achieved by detecting the impedance change of the coil.

According to the characteristics of the eddy current effect, it can be described using a transformer model. As shown in Fig. 3, the characteristics of both the probe coil and the detection surface can be represented by series-connected resistors and inductors, serving as the primary and secondary sides of the transformer, respectively. The magnetic coupling caused by the eddy current effect can be characterized by the mutual inductance between the primary and secondary sides. This circuit can be

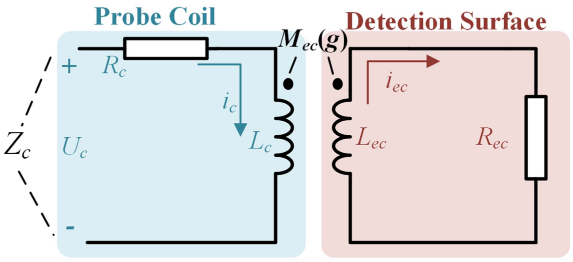

Fig. 3. Transformer model of the ECS.

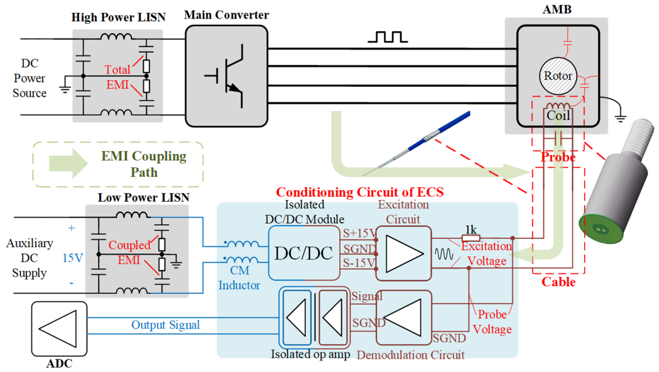

Fig. 4. System structure of the ECS and the AMB.

described by

$$\begin{cases} U_c = R_c i_c + j\omega L_c i_c - j\omega M_{ec} i_{ec} \\ 0 = R_{ec} i_{ec} + j\omega L_{ec} i_{ec} - j\omega M_{ec} i_c \end{cases} . \tag{2}$$

Then, the equivalent impedance of the primary side Z_c can be presented by

$$Z_c(\omega, g) = R_c + k(\omega, g) R_{ec} + j\omega [L_c - k(\omega, g) L_{ec}] \tag{3}$$

where

$$k(\omega, g) = \frac{\omega^2 M_{ec}(g)^2}{R_{ec}^2 + (\omega L_{ec})^2}.$$

Thus, it can be defined that

$$\begin{cases} R^*(\omega, g) \triangleq R_c + k(\omega, g) R_{ec} \\ L^*(\omega, g) \triangleq L_c - k(\omega, g) L_{ec} \end{cases} . \tag{4}$$

The eddy current effect introduces an extra positive resistance and negative inductance. The factor k is a function of both ω and g, but at a specific distance, it can be approximated as a constant within the high-frequency range.

B. System Structure and EMI Coupling Path of the ECS

The system structure where the ECS is implemented in the AMB system is shown in Fig. 4. The AMB platform in this article is a typical two-DOF eight-pole radial bearing and it is driven by a four-leg converter as has been presented in [9].

To study the propagation path of EMI in ECS, we designed a prototype based on its working principles, including the probe, cable, and conditioning circuits. The cable is a coaxial cable with a shielding layer. And its characteristic impedance is 50 Ω. In the conditioning circuit, the excitation circuit generates a high-frequency sinusoidal excitation voltage of 2 MHz, an 1 kΩ resistor is used to divide the voltage with the probe, converting the changes in the probe impedance into changes in the probe voltage. The demodulation circuit performs peak detection on the probe voltage. An isolated dc–dc module serves as power supply of the ECS, and an isolated Op-Amp is used to isolate the sensor from the external circuits. Additionally, a CM inductor is configured at the power input to suppress the propagation of CM EMI in the ECS.

As illustrated in Fig. 4, the interference experienced by the sensor primarily originates from two sources. First, the switching of the converter will induce a high-frequency voltage on the AMB frame and rotor. Since the probe of the ECS is mounted on the frame and the coil faces directly towards the rotor surface, these high-frequency interference will conduct into the coil through the stray capacitors. Second, the radiated EMI in the space will induce an interference voltage on the shielding layer of the coaxial cable. Note that the radiated EMI could be mainly contributed from CM EMI on the cable of AMB drive [26], thus, the DM EMI of the AMB system will seldomly influence the sensor. These two interference sources will form interference currents through the excitation circuit, isolated dc–dc module, and CM inductor, thereby affecting the normal measurement of the sensor. It is worth noting that the demodulation circuit hardly conducts EMI, because the EMI coupled from the input stage of the Op-Amp can be omitted as will be addressed later. To measure the total EMI of the whole system and also the coupled EMI in ECS, LISNs are added at the power supply sides of both the main circuit and the ECS.

Since the interference on the ECS comes from both conducted and radiated EMI, it will be in a super wide frequency range. However, the excitation frequency of the sensor is usually set between several hundred kHz and 10 MHz, with a highest 22 MHz found in [23], thus, the EMI within in 150 kHz-30 MHz will superimpose with the excitation signal and significantly affecting its normal operation. For higher-frequency radiated EMI (above 30 MHz), due to its much higher frequency than excitation signal, its effect can be easily eliminated by low-pass or band-pass filter as has been proposed in [22] and [23]. Therefore, this article only cares about the coupled EMI below 30 MHz, which include the conducted EMI and low-frequency radiated EMI, as illustrated in [26].

III. CONDUCTING MODEL OF EMI IN ECS

To quantitatively analyze the propagation characteristics of EMI in the ECS, it is necessary to construct high-frequency models for each component, including the probe, cable, Op-Amp-based excitation circuit, dc–dc power module, CM inductor, and LISN, which will be introduced separately.

A. High-Frequency Model of the Probe

The probe of the ECS includes a coil, a capacitor, and an iron shell. The parallel capacitor is used to resonate with the coil, increasing the variation amplitude of the probe impedance

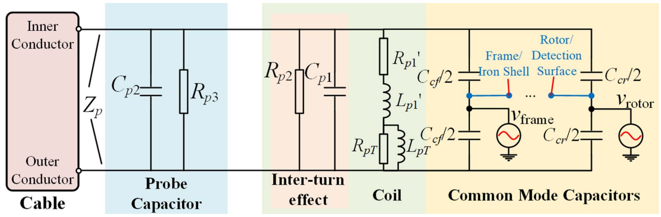

Fig. 5. Lumped parameter equivalent circuit of the ECS probe.

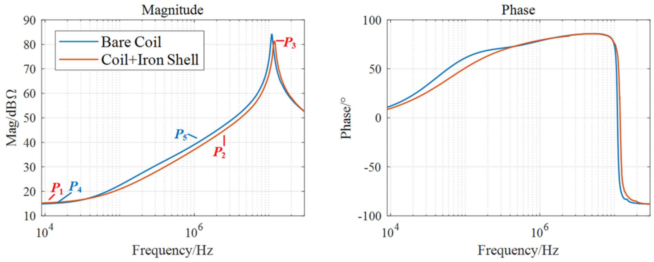

Fig. 6. Measured impedance of coil with iron shell.

caused by the detection distance, thereby enhancing the sensitivity of displacement measurement. The iron shell is used to fix the probe coil onto the frame of the AMB. The ECS is used to measure the displacement of the rotor, thus, the rotor surface serves as the detection surface of the sensor.

The lumped parameter equivalent circuit of the entire probe is shown in Fig. 5. The probe capacitance C_{p2} along with its equivalent parallel resistance R_{p3} can be measured directly. The equivalent model of the coil includes a series *RL* branch representing the winding and a parallel *RC* branch representing the interturn effect. Specifically, $R_{p1}{}'$ and $L_{p1}{}'$ are both composed of three parts

$$\begin{cases} R_{p1}{}' = R_c + \Delta R_{cf} + \Delta R_{cr} \\ L_{p1}{}' = L_c - \Delta L_{cf} - \Delta L_{cr} \end{cases} \tag{5}$$

where R_c and L_c are the original resistance and inductance of the coil, ΔR_{cf} and ΔL_{cf} are the additional resistance and inductance introduced by the magnetic coupling between the iron shell and the coil, and ΔR_{cr} and ΔL_{cr} are introduced by the eddy current effect with the detection surface. Also, the paralleled R_{pT} and L_{pT} are set to represent the skin effect of the eddy current effect.

Fig. 6 shows the measured impedances of the bare coil and coil plus iron shell. It can be seen that the iron shell can indeed change the *RL* characteristics of the coil. Some parameters of the coil can be decided by the measured results

$$\begin{cases} R_c \simeq \mathrm{Re}(Z_{P1}),\ R_c + \Delta R_{cf} \simeq \mathrm{Re}(Z_{P4}) \\ L_c \simeq \dfrac{\mathrm{Im}(Z_{P2})}{2\pi f_{P2}}, L_c - \Delta L_{cf} \simeq \dfrac{\mathrm{Im}(Z_{P5})}{2\pi f_{P5}} \\ C_{p1} \simeq \dfrac{1}{L_c(2\pi f_{P3})^2},\ R_{p2} \simeq \mathrm{Re}(Z_{P3}). \end{cases} \tag{6}$$

Next, the differential mode (DM) impedances of the probe (Z_p) were measured at different air gap g, the results are shown in Fig. 7. It can be seen that the eddy current effect will increase the low-frequency impedance and reduce the impedance in mid frequency range, which is consistent with the transformer model

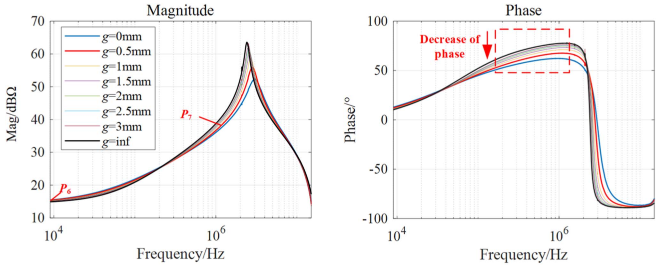

Fig. 7. Impedance of the probe under different g.

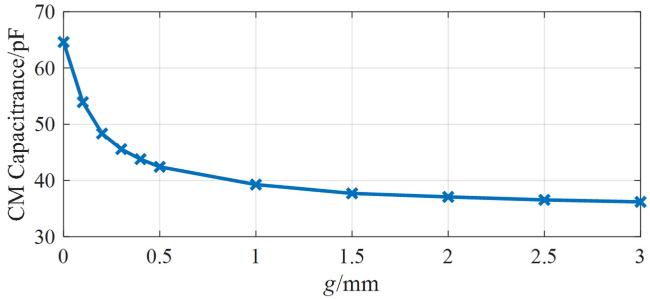

Fig. 8. CM capacitance between the probe and the detection surface.

mentioned earlier, resulting in ΔR_{cr} and ΔL_{cr} in (5). More importantly, as g decreases, the phase of the mid frequency band significantly decreases, which is caused by the skin effect. Only using series *RL* branch cannot characterize the skin effect, thus, the paralleled R_{pT} and L_{pT} are essential for the model. Taking $g = 0.5$ mm as a typical example to build the model for the ECS, note that all modeling work below is under this condition. The remaining parameters of the equivalent circuit of the coil can be calculated based on the measurement results

$$\begin{cases} R_{p1}{}' = \mathrm{Re}(Z_{P6}),\ R_{p1}{}' + R_{pT} = \mathrm{Re}(Z_{P7}) \\ L_{p1}{}' + L_{pT} = \dfrac{\mathrm{Im}(Z_{P6})}{2\pi f_{P6}},\ L_{p1}{}' = \dfrac{\mathrm{Im}(Z_{P7})}{2\pi f_{P7}}. \end{cases} \tag{7}$$

Then, the CM capacitance between the probe and the detection surface is tested and shown in Fig. 8, it can be seen that the CM capacitance decrease with the increase of distance g. Note that the CM capacitances are measured on condition that the probe is mounted on a calibrator, thus, the iron shell are connected with the detection target, and the measured capacitance is $C_{cf}+C_{cr}$. The C_{cf} can be decided by set $g\approx\infty$.

The predicted impedances of the probe model are compared with the measured results, which is shown in Fig. 9. When g is set as ∞, there's no eddy current effect, the model fit well with the measured results. When the eddy current effect is taken into consideration at $g = 0.5$ mm, ΔR_{cr}, ΔL_{cr},R_{pT}, and L_{pT} are added to the model, which still turns out to fit well with the measured results.

B. Model of the Shielded Coaxial Cable

The signal transmission of commercial ECSs typically uses the shielded triaxial cable, whose cross-sectional diagram is

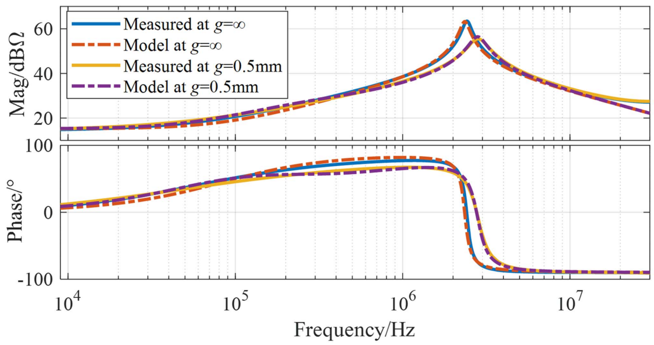

Fig. 9. Comparison between predicted and measured impedance.

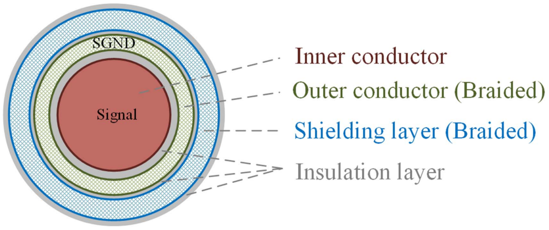

Fig. 10. Cross-sectional diagram of the triaxial cable.

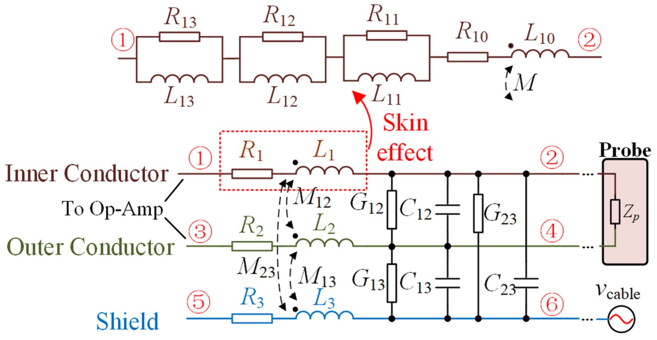

Fig. 11. Lumped parameter equivalent circuit of one cable segment.

shown in Fig. 10. It mainly includes the inner signal layer, the outer signal layer, and the shielding layer. Sensor cables are usually several meters long. When considering the frequency band of up to 30 MHz, the transmission line characteristics resulting from the distributed parameter properties must be considered. A typical way to cope with this is to piece together multiple lumped parameter circuit segments, as presented in [27] and [28]. According to the multiconductor transmission line theory [29], [30], the equivalent circuit segment of the triaxial cable is shown in Fig. 11. The length of the cable of the ECS is 4 m, and its model is divided into 8 segments with 0.5 m for each one.

As shown by Fig. 10, the inner conductor is concentric wire, so that the skin effect cannot be ignored in high-frequency range. Therefore, three parallel *RL* brunches are added to the model of inner conductor to fit its frequency dependent feature. The parameters in Fig. 11 can be extracted with either finite element tools [29] or network fitting [30]. For the sake of efficiency and simplicity, this article adopts the method of port impedance measurement to extract the parameters. Three sets of tests were conducted, as listed in Table I.

TABLE I
LIST OF TEST CONFIGURATIONS

Testing Sets	Test Points		
Test of L and R ($Z_{LR\text{-}i}$)	①,②	③,④	⑤,⑥
Short circuit tests ($Z_{SH\text{-}ij}$)	①,③ (②④shorted)	①,⑤ (②⑥shorted)	③,⑤ (④⑥shorted)
Open circuit tests ($Z_{OP\text{-}ij}$)	①,③ (②④open)	①,⑤ (②⑥open)	③,⑤ (④⑥open)

In Table I, the subscripts i and j represent the conductor numbers, where "1" denotes the inner conductor, "2" denotes the outer conductor, and "3" denotes the shielding layer. Based on the test results of $Z_{LR\text{-}i}$, the inductance and resistance of the conductors can be calculated by

$$\begin{cases} R_i(\omega) = \mathrm{Re}[Z_{LR-i}(j\omega)] \\ L_i(\omega) = \mathrm{Im}[Z_{LR-i}(j\omega)]/\omega \end{cases}. \tag{8}$$

The tested $Z_{SH\text{-}ij}$ can be presented as

$$\begin{aligned} Z_{SH-ij}(j\omega) = {} & R_i(\omega) + R_j(\omega) \\ & + j\omega[L_i(\omega) + L_j(\omega) - 2M_{ij}(\omega)]. \end{aligned} \tag{9}$$

Then, the mutual inductances can be solved as

$$M_{ij}(\omega) = \frac{L_i(\omega) + L_j(\omega) - \mathrm{Im}[Z_{SH-ij}(j\omega)]/\omega}{2}. \tag{10}$$

The tested $Z_{OP\text{-}ij}$ can be presented as

$$\begin{cases} Z_{OP-12}(j\omega) = \frac{(Z_{CG-13}+Z_{CG-23})Z_{CG-12}}{Z_{CG-12}+Z_{CG-13}+Z_{CG-23}} + Z_{SH-12} \\ Z_{OP-13}(j\omega) = \frac{(Z_{CG-12}+Z_{CG-23})Z_{CG-13}}{Z_{CG-12}+Z_{CG-13}+Z_{CG-23}} + Z_{SH-13} \\ Z_{OP-23}(j\omega) = \frac{(Z_{CG-12}+Z_{CG-13})Z_{CG-23}}{Z_{CG-12}+Z_{CG-13}+Z_{CG-23}} + Z_{SH-23} \end{cases} \tag{11}$$

where $Z_{CG\text{-}ij}$ is the paralleled impedance of G_{ij} and C_{ij}. Since the amplitude of Z_{SH} is far smaller than that of Z_{OP}, they are omitted so that Z_{CG} can be solved as

$$\begin{cases} Z_{\mathrm{CG}-12}(j\omega) = \frac{a^2-2ab+b^2-2ac-2bc+c^2}{2(a-b-c)} \\ Z_{\mathrm{CG}-13}(j\omega) = \frac{-a^2+2ab-b^2+2ac+2bc-c^2}{2(a-b+c)} \\ Z_{\mathrm{CG}-23}(j\omega) = \frac{-a^2+2ab-b^2+2ac+2bc-c^2}{2(a+b-c)} \end{cases} \tag{12}$$

where $a = Z_{OP\text{-}12}(j\omega)$, $b = Z_{OP\text{-}13}(j\omega)$, $c = Z_{OP\text{-}23}(j\omega)$. The C and G can be calculated by

$$C_{ij}(\omega) = \frac{-\mathrm{Im}[Z_{\mathrm{CG}-ij}(j\omega)]}{\mathrm{abs}[Z_{\mathrm{CG}-ij}(j\omega)]^2\omega},\ G_{ij}(\omega) = \frac{\mathrm{Re}[Z_{\mathrm{CG}-ij}(j\omega)]}{\mathrm{abs}[Z_{\mathrm{CG}-ij}(j\omega)]^2}. \tag{13}$$

All the solved parameters are listed in the appendix. Note that the conductance parameters G_{ij} are very small and, thus, has been ignored. Then, the frequency dependent R_1 and L_1 are fitted with R_{10}~R_{13}, L_{10}~L_{13} shown in Fig. 11. The fitted results are shown in Fig. 12. By connecting single-segment lumped parameter equivalent models end-to-end, a complete transmission line equivalent model is obtained. Impedance measurements are

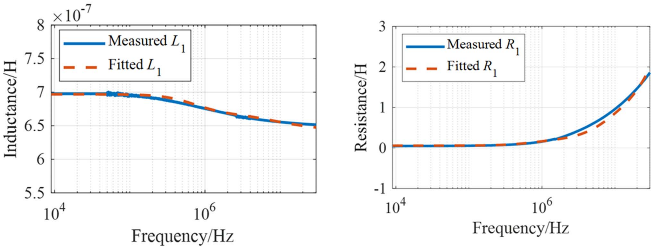

Fig. 12. Fitting results of L_1 and R_1.

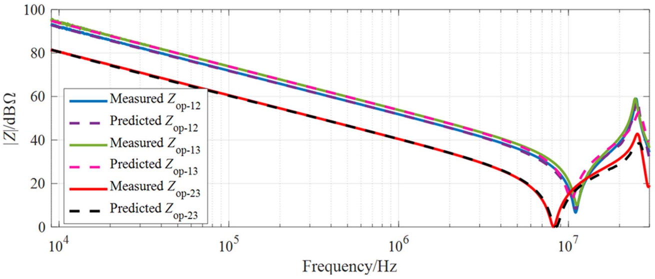

Fig. 13. Comparison of predicted and measured impedance of the cable.

taken at the end of the entire cable when it is open-circuited. A comparison with the model's predicted results, as shown in Fig. 13, demonstrates the accuracy of the cable model.

C. Model of the Excitation Circuits

The excitation circuit of the ECS is built based on Op-Amps and their power supplies. A crystal oscillator generates a fixed-frequency pulse signal (2 MHz in this article), which is filtered and amplified to ultimately form a sinusoidal excitation signal. Typically, Op-Amps and isolated dc–dc power supply are packaged chips or modules to reduce the sensor's size, thus, their detailed internal structures and technical parameters are usually not disclosed to users. Therefore, it is not possible to construct transistor-level simulation models, and behavioral models are needed.

Regarding the EMI issue of Op-Amps, the nonlinear demodulation and high-frequency models proposed by Fiori and Crovetti [15] and Quitadamo and Fiori [16] essentially depend on stray parameters brought about by semiconductor structures and packaging, mainly including a few pF of capacitance and a few nH of inductance. The effective frequencies of these models are in the range of hundreds of MHz to GHz, and significant effects are only noticeable when the high-frequency interference voltage amplitude exceeds several hundred mV. This is almost negligible in power electronics-driven AMB systems.

More importantly, these models assume the Op-Amp's GND as a constant zero potential, thus, the EMI will affect the Op-Amp's DM output characteristics. When Op-Amps are applied to power electronic systems, things turn out to be different. In AMB systems, only the protection earth can be considered as constant zero potential. And the EMI flowed through the Op-Amp and conducted along its power supply is the main issue affecting the ECS. This type of interference almost does not affect the normal operation of the Op-Amps but will still influence the entire ECS system.

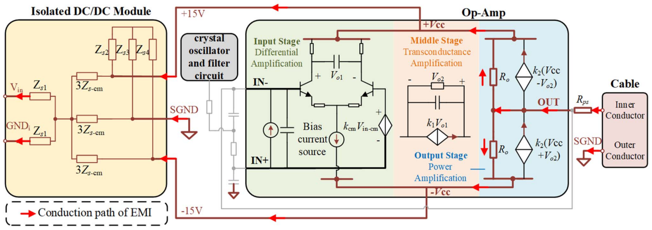

Fig. 14. Macro model of the Op-Amp based condition circuit.

This phenomenon can be illustrated with the use of macro model of the Op-Amp, as shown in Fig. 14. The model is composed of input, middle, and output stage. The input stage is a differential amplifier circuit, which characterizes the Op-Amp's ability to pass through DM signal and suppress CM input voltage. In this stage, the DM input signal will obtain a unity gain, and the suppression ratio of CM signals can be set by changing the value of k_{cm}. In this article, k_{cm} is set to 10^{-6}, corresponding to the 120 dB CM rejection ratio provided by the datasheet. The middle stage is an *RC*-filtered transconductance amplifier, representing the Op-Amp's open-loop amplification gain and its bandwidth. The amplifier is characterized by a voltage controlled current source, with a transconductance gain of 80 dB, corresponding to the dc gain of the Op-Amp. The bandwidth of the *RC* low-pass filter is set to 10 kHz, corresponding to the open-loop bandwidth of the Op-Amp. The output stage is a push–pull power amplifier, characterized by low output impedance. The k_2 is set as $1/R_0$ to realize unit voltage gain. This model can characterize the basic impedance characteristics of each port and the correlation between port signals of the Op-Amp. Other features and circuits within the Op-Amp, such as the bias current source circuit, multistage transconductance amplifier circuits, saturation, and current limiting circuits, are irrelevant to the simulation of conducted EMI and are therefore ignored. Negative feedback is introduced through the *RC* network outside the macro model, together forms an active second-order low-pass filter. The 5 V square wave signal generated by the crystal oscillator will first pass through a passive filtering network, and then through this active filter to finally generate a 2 MHz low output impedance sine excitation signal.

The CM EMI couples into the excitation circuit of the ECS through the sensor probe and cable, and conducted through R_o to the *Vcc* ports of the Op-Amp, and then coupled to the output end of the isolated dc–dc module. Due to the small value of R_o, the closed-loop output characteristics of the operational amplifier are almost unaffected. In fact, in our experiments, no significant interference was observed in the excitation signal of the ECS even under the worst conditions.

For some Op-Amps, the manufacturer provides macro models and their specific parameters. When a complete macro model is not available, it can still be constructed using the open-loop gain, CM rejection ratio, open-loop amplification bandwidth, and other data provided in the datasheet. Additionally, the R_o

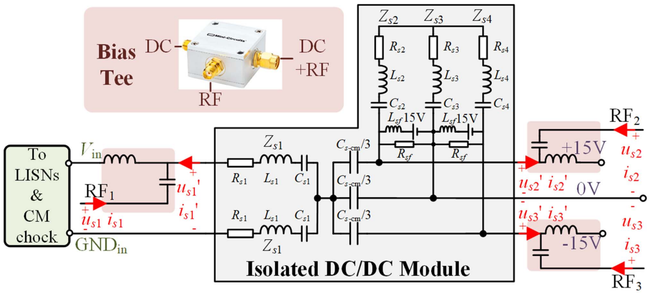

Fig. 15. Behavioral model of DC–DC module and online measurement setups.

parameter, which is crucial for conducted EMI, can be obtained through offline measurement.

D. Model of the Isolated DC–DC Module

For the isolated dc–dc module, it is necessary to establish its behavioral model. Since the structure and topology of the module are unknown, behavior model based on multiterminal network theory [31], [32] is built, as shown in Fig. 15. Note that the voltage level of the dc–dc module is much lower than that of the AMB controller, so the EMI caused by high-frequency switching devices inside the module can be ignored. Another proof of this is that when the power supply of the ECS is turned ON without operating the AMB, there is no interference in the sensor signals. The DM impedance of the primary side is represented by Z_{s1}, while that of secondary side is presented by star-connected Z_{s2}, Z_{s3}, and Z_{s4}, the CM characteristic is presented by three star-connected $C_{s\text{-cm}}$. To still retain the low-frequency output voltage characteristics of the dc–dc converter, two ideal 15 V voltage sources are added at its output and they are connected to the high-frequency equivalent circuit through a large coupling inductor L_{sf}. Additionally, large parallel resistors R_{sf} are added to enable the dc–dc module's output ports to be connected to inductive loads.

The parameters in Fig. 15 should be extracted with online network measurements since the input impedances of the module ports change a lot under different working conditions. Bias-tees are used to inject RF signals into the dc-powered system, thereby extracting the system's scattering parameters (*S* parameters). Note that the CM capacitor $C_{s\text{-cm}}$ was founded to be nearly unchanged with offline or online measurement, thus, only the DM impedances Z_{s1}–Z_{s4} should be measured online.

First, the *S* parameters of the bias-tee are measured with vector network analyzer and transformed to *ABCD* parameters, as presented by

$$\begin{bmatrix} u_{si} \\ i_{si} \end{bmatrix} = \begin{bmatrix} A & B \\ C & D \end{bmatrix} \begin{bmatrix} u_{si}' \\ -i_{si}' \end{bmatrix}, \quad (i = 1, 2, 3). \tag{14}$$

Then, the *S* parameters of the whole system are measured and transformed to *Z* parameters as

$$\begin{bmatrix} u_{s1} \\ u_{s2} \\ u_{s3} \end{bmatrix} = \begin{bmatrix} Z_{s11} & Z_{s12} & Z_{s13} \\ Z_{s21} & Z_{s22} & Z_{s23} \\ Z_{s31} & Z_{s32} & Z_{s33} \end{bmatrix} \begin{bmatrix} i_{s1} \\ i_{s2} \\ i_{s3} \end{bmatrix}. \tag{15}$$

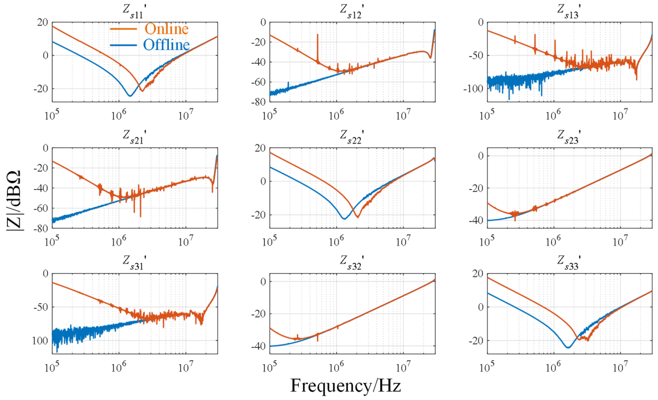

Fig. 16. Measured *Z* parameters of DC–DC module.

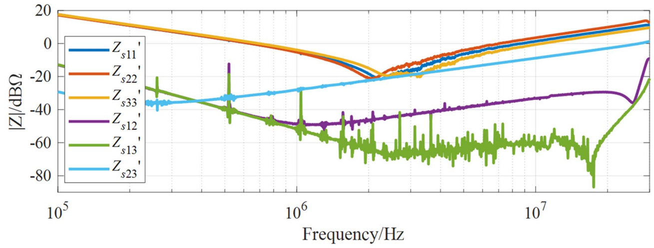

Fig. 17. Comparison of online measured *Z* parameters.

Based on (14) and (15), the *Z* parameters of the dc–dc module can be calculated by

$$\boldsymbol{U}_s{}' = \boldsymbol{Z}_s{}'\boldsymbol{I}_s{}' = (C\boldsymbol{Z}_s - A\boldsymbol{E})^{-1}(D\boldsymbol{Z}_s - B\boldsymbol{E})\boldsymbol{I}_s{}' \tag{16}$$

where $\boldsymbol{I}_s{}' = [i_{s1}{}'\ i_{s2}{}'\ i_{s3}{}']^T$, $\boldsymbol{U}_s{}' = [u_{s1}{}'\ u_{s2}{}'\ u_{s3}{}']^T$, $\boldsymbol{Z}_s$ is the *Z* parameter matrix in (15), $\boldsymbol{E}$ is the third-order identity matrix.

The measured results of the *Z* parameters of the dc–dc module under both online and offline condition are plotted and compared in Fig. 16. The online impedances are significantly different from offline measured results. Also, the online measured impedances are plotted in one figure, as shown in Fig. 17. It can be seen that the magnitude of $Z_{s12}{}'$ and $Z_{s13}{}'$ are far smaller than that of other parameters, which means that the DM voltage of the primary side does not affect the secondary side, and vice versa, so that we do not need to build a DM coupling path between the two sides in the model.

Based on the measured results, the impedances in the behavior model can be set as

$$\begin{cases} Z_{s1} = Z_{s11}{}'/2, \ Z_{s2} = Z_{s22}{}' - Z_{s23}{}' \\ Z_{s3} = Z_{s23}{}', \ Z_{s4} = Z_{s33}{}' - Z_{s23}{}' \end{cases}. \tag{17}$$

The *RLC* branches are used to fit the measured impedances, the fitting results are shown in Fig. 18.

E. Model of the CM Inductor and LISN

A CM inductor is added at the power input of the ECS's conditioning circuit to reduce conducted CM EMI. Additionally, LISNs are included to ensure the stability of the measurement impedance. These are typical passive components, and their

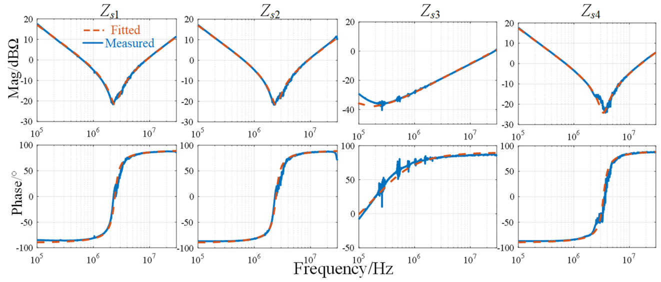

Fig. 18. Fitting results of impedances in DC–DC module.

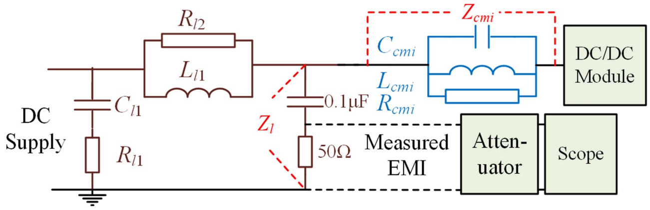

Fig. 19. Equivalent model of LISN and CM inductor.

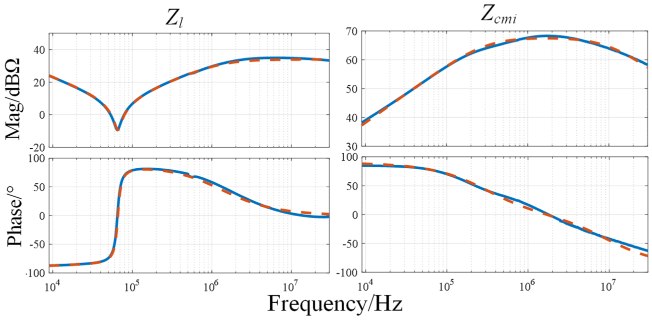

Fig. 20. Fitted results of LISN and CM inductor.

equivalent models are shown in Fig. 19. The impedance fitting results obtained from the measurements are shown in Fig. 20.

Till now, the model for the ESC has been well established, which can be used for time domain simulation. Note that all the parameters of the models mentioned above are listed in the appendix.

IV. EXPERIMENTAL VALIDATION OF THE PROPOSED MODEL

The experiments based on ECS prototype and AMB platforms are carried out to verify the accuracy of the proposed high-frequency model of the ECS. The experiment configurations are shown in Fig. 21.

The ECS probe is mounted on the calibrator to maintain a constant detection distance g of 0.5 mm in all experiments. The calibrator is connected directly with the frame of a two-DOF radial AMB, thus, the probe iron shell and the detection surface have the same voltage as the AMB frame. The RF terminals of the two LISNs on the power supply side of the ECS are connected to a CM/DM separation module. The resulting CM voltage signals can be observed using an oscilloscope. The frequency domain CM EMI coupled to the sensor can be tested with an EMI receiver using EZ-17 current probe clamped on the DUT side of the low power LISNs. The dc bus voltage of the AMB controller is set as 150 V, and the switching frequency is set as 20 kHz. The dc bias currents of all the AMB windings are set as 2.4 A. All experiments were conducted under the static suspension condition of the AMB.

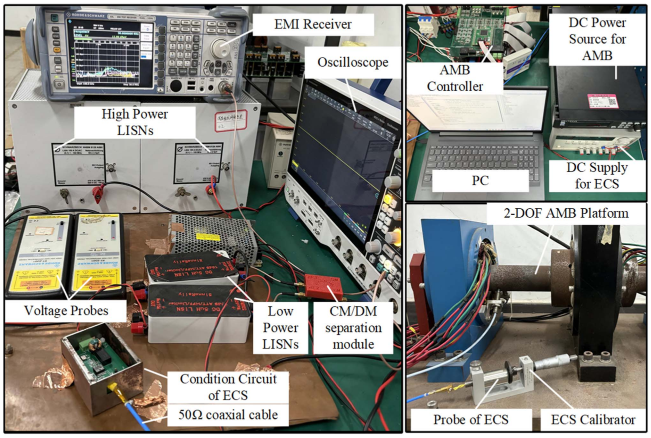

Fig. 21. Experiment Platform.

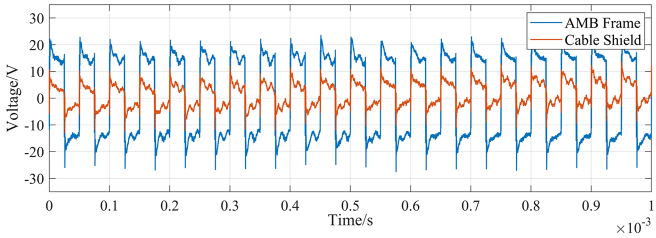

Fig. 22. Measured voltage on AMB frame and cable shield.

The previously constructed high-frequency model of the ECS is simulated in the time domain. A 2 MHz 5 V square wave signal as generated by the crystal oscillator is used as the input to the ECS's conditioning circuit, allowing for the simulation of its basic operating characteristics. As analyzed before, the interference of the ECS mainly comes from two sources. According to the substitution theorem of circuits, the measured frame voltage of the AMB and the voltage on the cable shield layer are used as inputs to the simulation model to simulate the high-frequency interference, as shown in Fig. 22. Since the experiment is done under static suspension condition of the AMB, the winding currents were approximately constant dc and the duty cycles of all bridge arms of the converter were almost the same, so that the CM voltage of the AMB drive is nearly like a square wave, and the induced voltage on the ECS cable shield and the AMB frame are also like square wave.

First, the CM EMI measured in the time domain is compared with the simulation results, as shown in Fig. 23. The measured CM EMI consists of three components: interference at 20 kHz caused by the switching of the AMB controller, interference at 250 kHz caused by the switching of the dc–dc module of the ECS, and interference at 2 MHz caused by the crystal oscillator of the excitation circuits. Among these, only the first component is the interference coupled from the power circuit to the sensor,

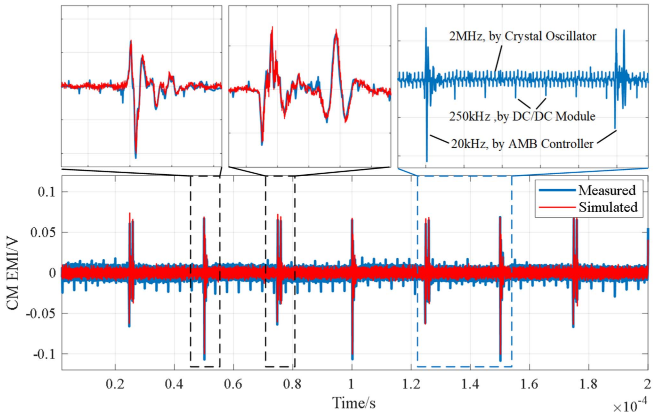

Fig. 23. Time domain comparison of measured and simulated EMI.

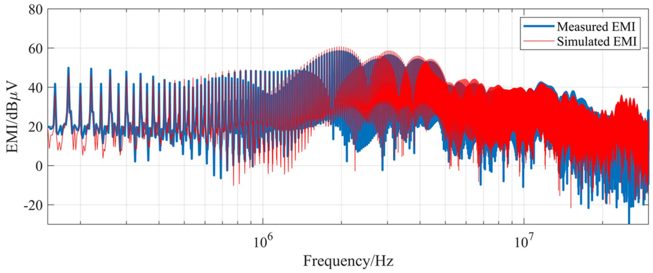

Fig. 24. Frequency domain comparison of measured and simulated EMI.

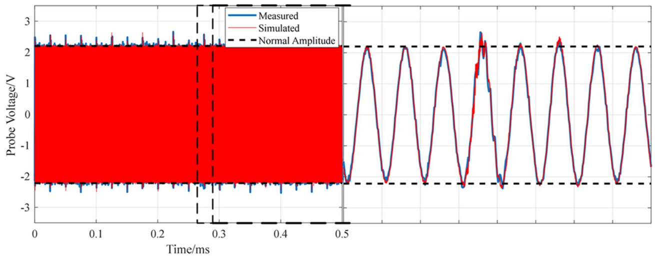

Fig. 25. Comparison between measured and simulated probe voltage.

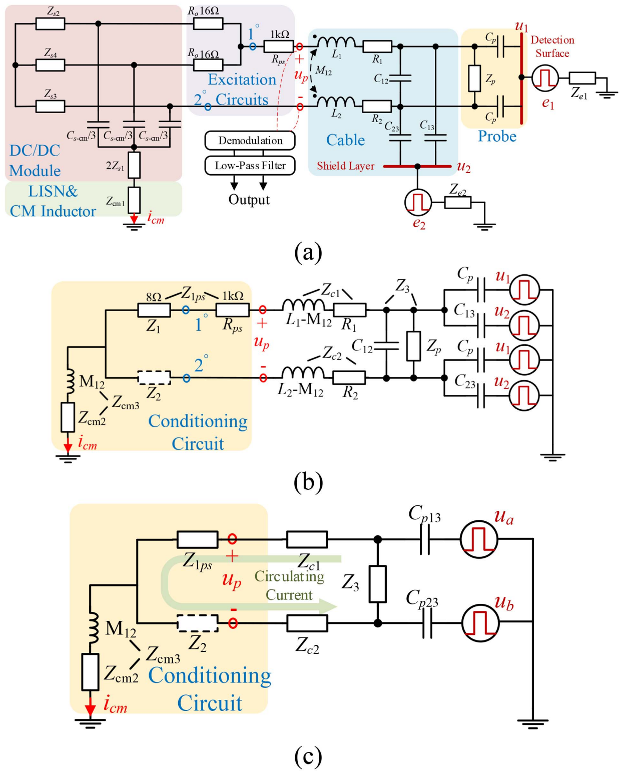

Fig. 26. Simplified equivalent circuit of the high-frequency ECS model: (a) simplified model, (b) further simplified, and (c) final model.

which has the largest amplitude, and only this component will affect the sensor's output signal. Therefore, the other two sources of interference are ignored in the simulation. Fig. 23 can validate that the simulation results match the experimental results very well in the time domain waveforms, exhibiting almost identical variation trends even during switching transients.

The frequency domain comparison of the measured and simulated EMI is shown in Fig. 24. It can be seen that the results match very well, with a maximum error of no more than 5 dB within 30 MHz.

Then, it is also necessary to verify whether the model can predict the effect of EMI on the sensor signals. Note again that no significant interference signal was observed on the sensor's excitation voltage during the experiment, but noticeable interference was present on the probe voltage (as defined in Fig. 4). Therefore, the measured and simulated probe voltages were compared, as shown in Fig. 25. When the detection distance g is fixed, the probe voltage is a constant amplitude sinusoidal voltage under normal conditions, but waveform distortion can be observed during each switching transient, and its peak-to-peak value also changes significantly. It can be seen that the model established in this article can well predict the signal distortion, further verifying the model's accuracy.

V. ANALYSIS OF MECHANISM OF CM EMI ON SENSOR SIGNALS

Based on the constructed high-frequency model, it is feasible to explain how the CM EMI will influence the output signal of the ECS, and how the high-frequency interference will affect the low-frequency displacement control loop.

A. High-Frequency Mechanism

Based on the previously established high-frequency model of the ECS, its simplified equivalent circuit is shown in Fig. 26(a). In this figure, the DM impedance of the probe is represented by Z_p, and C_p is the stray capacitance between the probe and the detection surface. Due to the complexity of the distributed parameter circuits of the cable, a one-segment *LC* equivalent model is used to simplify the analysis. R_o is the output resistance of the Op-Amp, as shown in Fig. 14, R_{ps} is the voltage divider resistor in series with the probe, and the impedances of the LISNs and CM inductors are collectively represented by $Z_{\text{cm}1}$. u_p is the probe voltage, which generates the output voltage signal

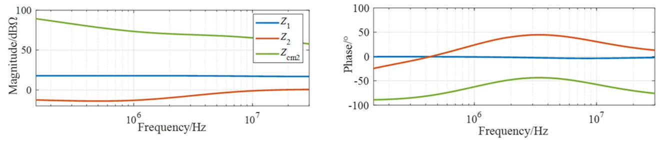

Fig. 27. Impedance of the equivalent star-connected circuit.

of the ECS after passing through the demodulation and low-pass filter circuits. The entire system includes two interference sources, which act on the detection surface and the cable shield, respectively, together generating the CM current i_{cm}.

The circuit in Fig. 26(a) can be further simplified and shown in Fig. 26(b). Port 1°, Port 2°, and GND together form a three-terminal network, which can be equivalently represented by the star-connected impedances Z_1, Z_2, and $Z_{\mathrm{cm}2}$. These three impedances can be measured from the simulation model and are shown in Fig. 27.

Among them, Z_1 is almost an 8 Ω resistor, Z_2 is very small and can be considered as short circuit, and $Z_{\mathrm{cm}2}$ has a very large magnitude, primarily determined by the CM capacitance of the isolation dc–dc module and the CM inductance. The coupling inductance of the cable can be decoupled into three independent inductances, L_1-M_{12}, L_2-M_{12}, and M_{12}. By merging all the series and parallel branches, the equivalent circuit is shown in Fig. 26(c), where

$$\begin{cases} C_{p13}=C_p+C_{13},\ C_{p23}=C_p+C_{23}\\ u_a=\frac{C_pu_1+C_{13}u_2}{C_p+C_{13}},\ u_b=\frac{C_pu_1+C_{23}u_2}{C_p+C_{23}}. \end{cases} \tag{18}$$

The model shown in Fig. 26(c) is a typical bridge circuit. It is still not easy to get the analytical solution for u_p with the two excitation sources, but it can be seen that u_p can be zero only when the bridge is balanced, which means that

$$\begin{cases} u_a=u_b, C_{p13}=C_{p23}\rightarrow C_{13}=C_{23}\\ Z_{c1}=Z_{c2}\\ Z_{1ps}=Z_2. \end{cases} \tag{19}$$

Formular (19) indicate that the system needs to be absolute symmetrical. However, obvious asymmetry can be found in the ECS prototype. The first part is because of the existing of the voltage divider resistor, which make Z_{1ps} much larger than Z_2. The other part is the asymmetry of the cable impedances, both the line inductance and the stay capacitance between difference cable layers are not the same. These asymmetries will cause circulating current, as shown in Fig. 26(c), that is the mechanism by which the CM EMI of the AMB system affects the DM sensor signal.

With the equivalent circuit model, we can get the transfer impedance $u_p(j\omega)/u_1(j\omega)$ and $u_p(j\omega)/u_2(j\omega)$ can be gotten in the simulation, as shown in Fig. 28(a), which can represent how the interference sources affect the probe voltage. In the low frequency range, the impedance of the propagation path of EMI is capacitive, so the transfer impedance is small and has a large amplitude above MHz as the frequency increases. With the measured voltages on the AMB frame and on the cable shield, the noise signal on the u_p can be calculated, as shown in Fig. 28(b).

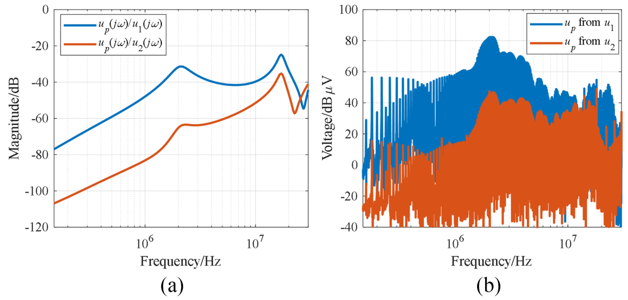

Fig. 28. Transfer impedance and the resulting noise on u_p. (a) Amplitude of transfer impedances. (b) Spectrum of noise on u_p.

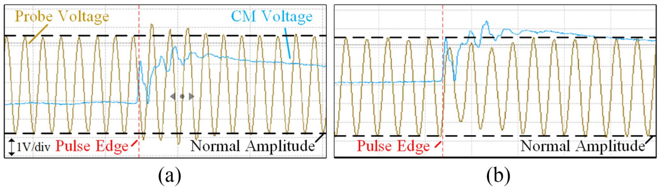

Fig. 29. Waveform of the CM voltage with the interfered probe voltage. (a) Increase of amplitude. (b) Decrease of amplitude.

It can be seen that the signal noise has a larger peak near several MHz, indicating that EMI in this frequency range is the main factor affecting the sensor; In addition, the voltage on the AMB frame is the main source of noise, while the radiated voltage on the cables mainly affects the high-frequency range.

B. Transformation of High-Frequency to Low-Frequency Interference

As has been shown in Fig. 25, the probe voltage distortion caused by pulse edges of CM voltage lasts only for two or three excitation sine wave cycles, corresponding to 1–2 μs. The bandwidth of the position loop control is generally within 1 kHz. It seems that a low-pass filter could effectively extract the original signal from the high-frequency interference, but this is not true for ECSs.

Note that under static suspension, the CM voltage of the AMB controller can be approximately considered as a 20 kHz square wave. In the time domain, when the probe voltage is interfered, its amplitude may either increase or decrease, as shown in Fig. 29. This mainly depends on the phase relationship between the CM voltage pulse edges and the sensor probe voltage.

The frequency of the sensor's sinusoidal excitation signal is $f_e = 2$ MHz, and the frequency of the CM voltage is $f_{\mathrm{cm}} = 20$ kHz. Ideally, the f_e are integer multiple of f_{cm}, making their phase relationship fixed. However, due to unavoidable frequency deviations, f_e can not strictly integer multiple of f_{cm}. In this case, the phase between the CM voltage pulse edges and the sinusoidal probe voltage will continuously change, as shown in Fig. 30.

Assume that ideally $f_e = kf_{\mathrm{cm}}$, but there is actually a slight deviation in f_e, resulting in $f_{e1} = f_e + \Delta f$. The relative phase and

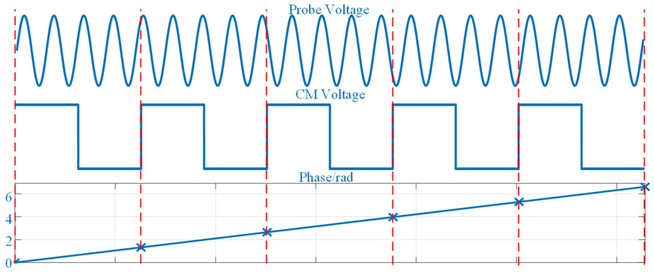

Fig. 30. Illustration of the phenomenon of phase shifting.

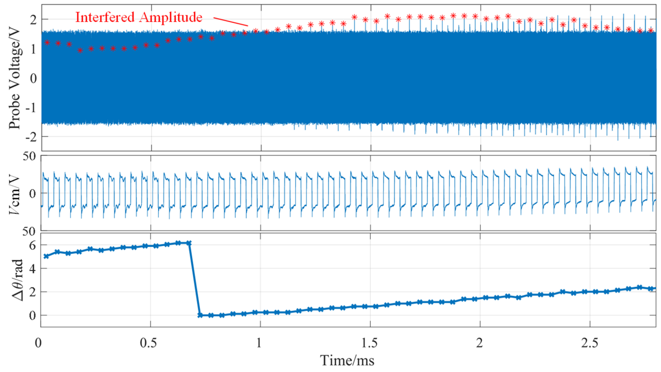

Fig. 31. Measured results to show the phase shift phenomenon.

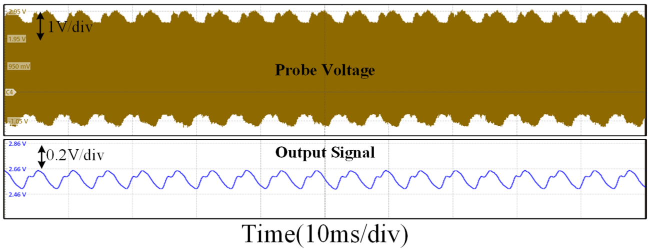

Fig. 32. Room-out waveform of the probe voltage and the output signal.

its variation frequency $f_{\Delta\theta}$ can then be expressed as

$$\Delta\theta(nT_{\text{cm}}) = 2n\pi\frac{1/f_{\text{cm}} - k/f_{e1}}{1/f_{e1}} = 2\pi n\frac{\Delta f}{f_{\text{cm}}},\ \ f_{\Delta\theta} = \Delta f. \tag{20}$$

Due to the periodic change of $\Delta\theta$, the amplitude of the probe voltage affected by EMI will also change periodically, whose frequency is also $f_{\Delta\theta}$. The experimental waveform of this phenomenon is shown in Fig. 31, which verifies that the phase between the rising edge of the CM voltage and the sinusoidal probe voltage changes linearly over time. The period of this variation is on the millisecond level, causing the interfered probe voltage amplitude to also change periodically at a low frequency.

The room out waveform of the probe voltage is shown in Fig. 32, and the output signal obtained after demodulation and low-pass filtering is also shown in Fig. 32, note the filter bandwidth is set as 1 kHz. Even when the detection distance of the ECS does not change, significant low-frequency fluctuation can be observed in the sensor's output signal, this phenomenon was also observed in [9] with commercial ECSs. The bandwidth of the AMB's position closed-loop is usually set to several hundred Hz, which will respond to such low-frequency interference, thereby affecting the normal suspension of the rotor.

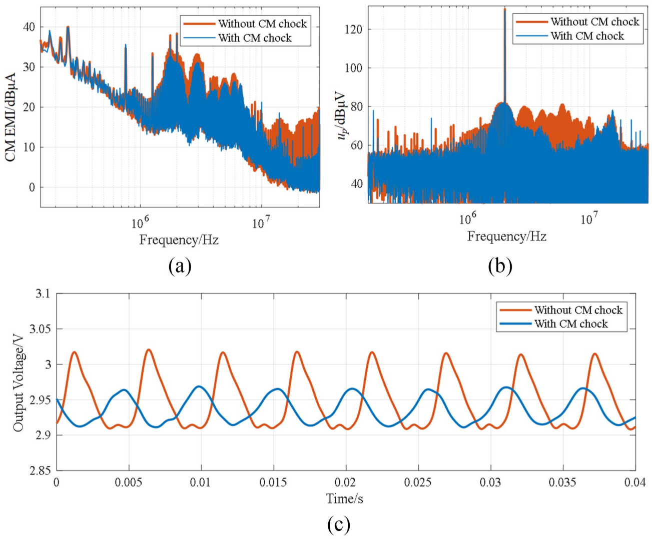

Fig. 33. Experiment results of adding CM chock. (a) CM EMI. (b) DM noise. (c) Output signal of the ECS.

VI. SUPPRESSION OF EMI EFFECTS IN ECS

Based on the above modeling and analysis of the ECS, the suppression methods are proposed and discussed in this section to enhance the EMC of the ECS.

A. *CM Chock, Shielding, and Grounding*

The interference experienced by ECSs mainly originates from the induced voltage on cable shield, AMB frame, and rotor. Typically, adding CM chokes in the transmission path can effectively suppress interference [33], [34]. The ECS prototype built in this article has already added a CM chock to its power supply side, thus, a comparative testing with or without this CM chock is conducted in experiments and the results are shown in Fig. 33.

Note that the CM EMI coupled to the ECS is measured on the LISNs located in the power supply side of the sensor. The DM EMI on these LISNs is meaningless, but as analyzed before, the noise on the probe voltage can represent for the DM noise of the sensor, thus this signal is measured and transferred to frequency domain. Also, the output signals of the ECS are measured to show the low-frequency interference. As can be shown in Fig. 33, with the CM chock, the CM EMI on the frequency range above 1 MHz is suppressed, thus, the DM noise caused by CM EMI also has a significant decrease. The amplitude of the low-frequency interference on the output signal is reduced by 53%. These results shows that the CM chock can effectively suppress the EMI effects on the ECS.

Reasonable shielding and grounding are also typical and effective means to suppress the EMI effects on the sensors. However, these methods have been found not always effective in ECSs, and would also render the CM chock ineffective.

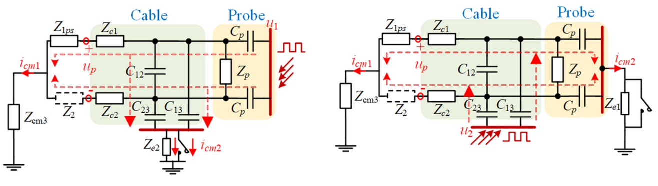

(a) (b)

Fig. 34. Equivalent circuit of ECS with (a) cable shield grounded and (b) detection surface grounded.

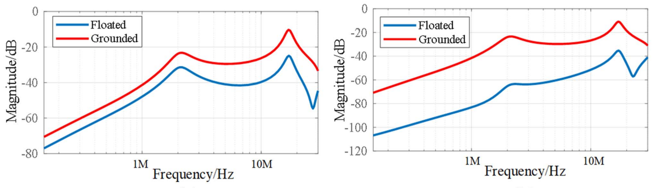

(a) (b)

Fig. 35. Frequency domain response of equivalent circuit of ECS. (a) $u_p(j\omega)/u_1(j\omega)$. (b) $u_p(j\omega)/u_2(j\omega)$.

We use the simplified equivalent circuit to illustrate this issue. First, we only consider the induced voltage u_1 on the detection surface, as shown in Fig. 34(a). There are two paths to conduct the CM current in the ECS. One is from the conditioning circuit to the power supply side of the ECS, as noted as i_{cm1}, another is from the cable to its shielding layer, noted as i_{cm2}. When the cable shield is not grounded, there is only a small stray capacitance between the cable shield and the reference ground, resulting in high impedance of Z_{e2}, thus, i_{cm2} is almost negligible. However, the grounding of the cable shield will provide a low-impedance path for i_{cm2}. Note that the high-frequency impedances of the capacitors between different conductors of the cable, C_{12}, C_{13}, and C_{23}, are much smaller than Z_{cm2}, and the capacitances will even increase with the length of the cable, so the grounding of cable shield will increase the CM current flowing into the ECS from the detection surface. This, in turn, will increase the DM circulating current in the conditioning circuit, worsening the interference to the probe voltage.

It is not easy to obtain analytical solution for circuit in Fig. 34(a), but the frequency domain numerical solution of $u_p(j\omega)/u_1(j\omega)$ can be obtained in simulation, as shown in Fig. 35(a). Note that when cable shield is floated, it is considered to be open to ground, and when it is grounded, it is considered to be short circuited to ground. It can be seen that when the cable shield is grounded, the interference brought to u_p by the voltage on detection surface will significantly increase.

Similarly, when consider the induced voltage on the cable shield, as shown in Fig. 35(b), the magnitude of $u_p(j\omega)/u_2(j\omega)$ is shown in Fig. 35(b). At this time, the interference brought to u_p by the voltage on cable shield will also significantly increase with the grounding of the detection surface.

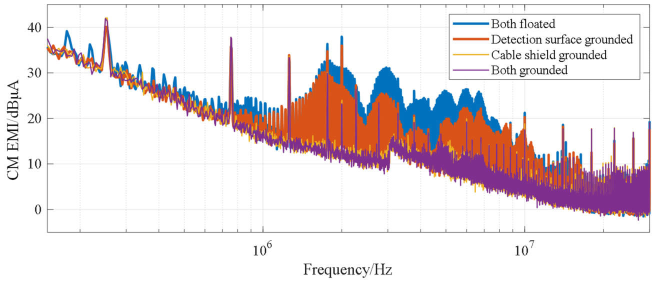

Fig. 36. Tested CM EMI under different grounding scheme.

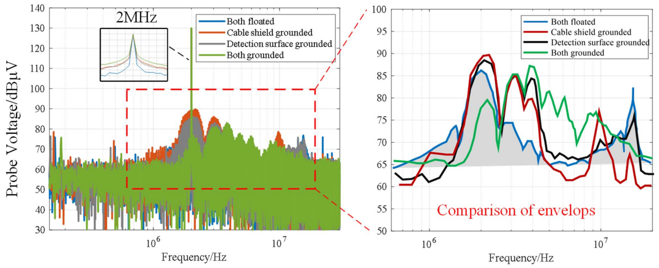

Fig. 37. Tested DM noise under different grounding scheme.

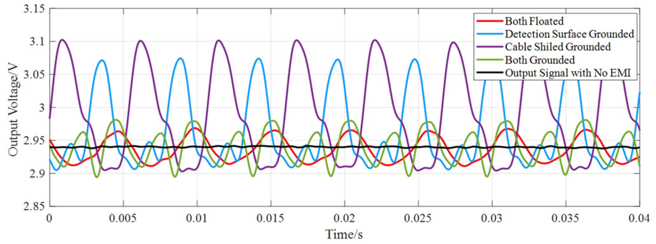

Fig. 38. Output signals of the ECS under different grounding configurations.

Consequently, grounding one of the two interference sources will increase the interference caused by the other source, possibly leading to greater interference on the probe voltage u_p compared to when both are floated. Ideally grounding the cable shield, frame, and rotor simultaneously could completely eliminate interference sources for the ECS, but this is not achievable in actual systems. Furthermore, since grounding will provide new low-impedance path for CM current, adding CM chock to the power supply and conditioning circuits of the ECS can only suppress i_{cm1} in Fig. 34, and thus, cannot effectively suppress the interference to u_p.

The experiments are carried out to verify the above analysis. Note that in experiments, the cable shield is grounded with copper foil which can be regarded as perfect grounding, while the frame of the AMB is grounded with wire. The CM EMI under different grounding scheme is shown in Fig. 36, the corresponding DM noise on the probe voltage is shown in Fig. 37, and the sensor output signals are shown in Fig. 38. It can be seen that every grounding scheme can decrease the amplitude of the coupled CM EMI compared with that when both are floated. However, the DM noise is not optimized and it is even deteriorated, the low-frequency interference on the output signals is also increased a lot. We may take the cable shield grounding as example. Under such condition, the CM currents i_{cm1} and i_{cm2}, as defined in Fig. 34(a), are measured in

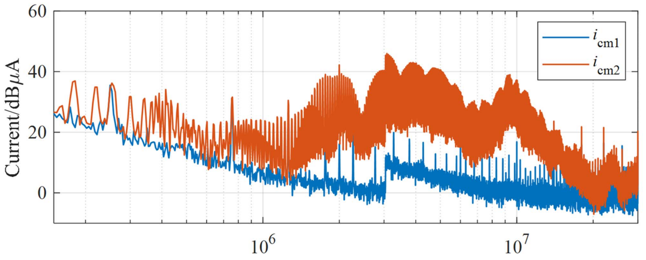

Fig. 39. Measured frequency domain waveform of $i_{\mathrm{cm}1}$ and $i_{\mathrm{cm}2}$ when cable shield is grounded.

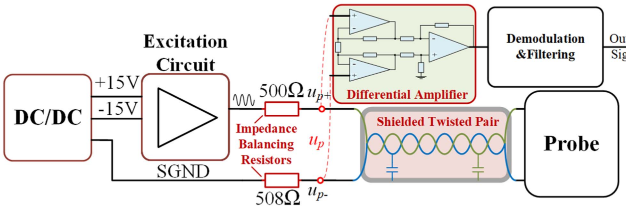

Fig. 40. Symmetrically designed ECS.

frequency domain and shown in Fig. 39. It can be seen that the grounding path of the cable shield passes through the majority of the CM current, which is because that C_{23} and C_{13} in Fig. 34(a) is much larger than C_p. Thus, $i_{\mathrm{cm}2}$ becomes the main factor that contribute to the interference on probe voltage. Even when both of them are grounded, the low-frequency error still cannot be suppressed effectively, this is mainly due to the fact that the grounding path is not ideal, so the optimization effect brought by grounding cannot compensate for the deterioration effect brought by the new low-impedance CM current path.

In order to better solve the problem of EMI in ECSs, two novel methods are proposed below, based on either the high-frequency mechanism or low-frequency mechanism.

B. Method Based on High-Frequency Mechanism

As has mentioned before, the high-frequency interference in the probe voltage u_p is mainly caused by the parameter asymmetries of the conditioning circuits and the cable. Therefore, we have proposed the symmetrical constraint for design of the ECS to suppress the influence of the CM EMI.

The circuit of the symmetrically designed ECS is shown in Fig. 40. First, the voltage divider resistance R_{ps} is divided into two parts, with 500 Ω in signal brunch and 508 Ω in SGND brunch. This extra 8 Ω is set to compensate the input resistance of the Op-Amp, so that Z_{1ps} in Fig. 26 can be nearly the same as Z_2. Then, to make the cable parameters to be symmetrical, the coaxial cable is replaced by shielded twisted pair with the same length. In this case, the line resistance and inductance of the two wires can be the same, and the stray capacitance between inner conductors and the shield can also be the same. Furthermore, differential amplifier circuit is needed before the demodulation circuit to detect the differential probe voltage u_p as well as to obtain a low output impedance.

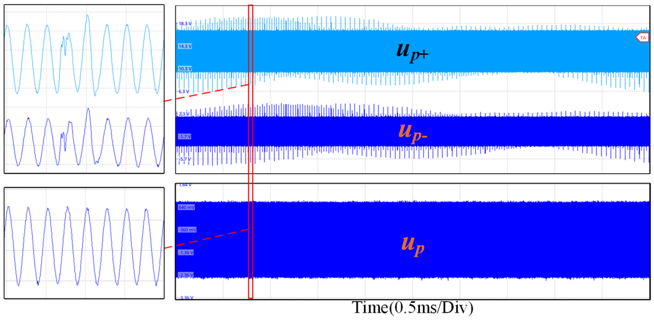

Fig. 41. Tested time domain u_p of the symmetrically designed ECS.

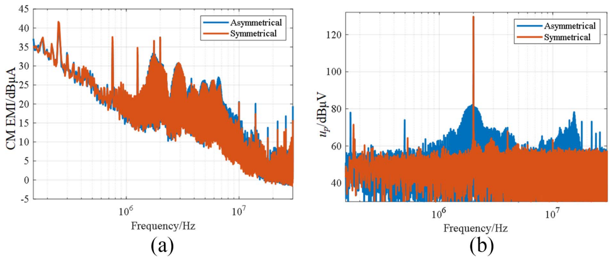

Fig. 42. Tested CM and DM EMI under symmetrical design. (a) CM EMI. (b) DM noise.

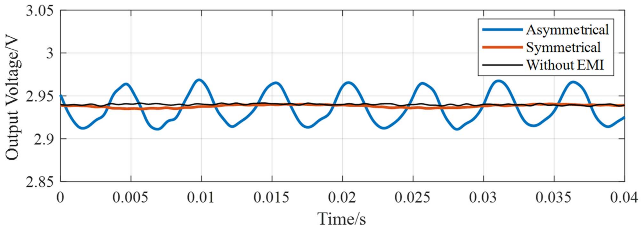

Fig. 43. Sensor's output signal under symmetrical design.

The prototype of the ECS based on the symmetrical design is then built and tested, the tested time domain probe voltage is shown in Fig. 41, the CM EMI and DM noise are shown in Fig. 42, the sensor's output signals are shown in Fig. 43. It can be seen from Fig. 41 that there are significant high-frequency interferences on u_{p+} and u_{p-}. However, due to the symmetrical design, the distortions on u_{p+} and u_{p-} are almost the same so that they can cancel each other, generating a differential probe voltage u_p with negligible distortion. It can be seen from Figs. 42 and 43 that the symmetrical design will not change the CM EMI, but it can almost completely eliminate the DM noise, resulting in negligible low-frequency variation on the output signal. These results indicate that the symmetrically designed ECS can keep unaffected even there is high amplitude CM EMI in the AMB system. This is an efficient and low-cost way to enhance the EMC of the ECS.

C. Method Based on Low-Frequency Mechanism

The low-frequency phase shift between the regularly varying CM voltage pulse edges and the sensor's excitation signal is the main cause of low-frequency interference in ECSs. If the

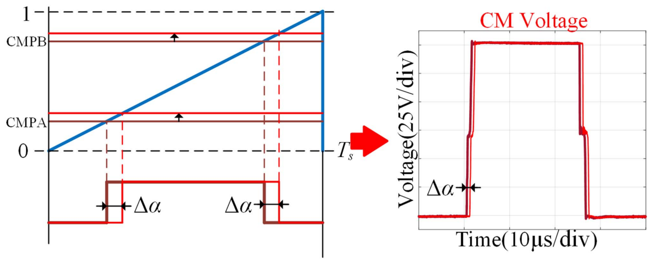

Fig. 44. Phase shifting of CM voltage.

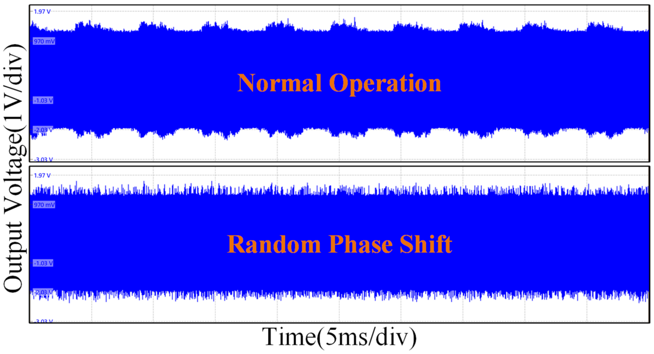

Fig. 45. Tested probe voltages under different modulation.

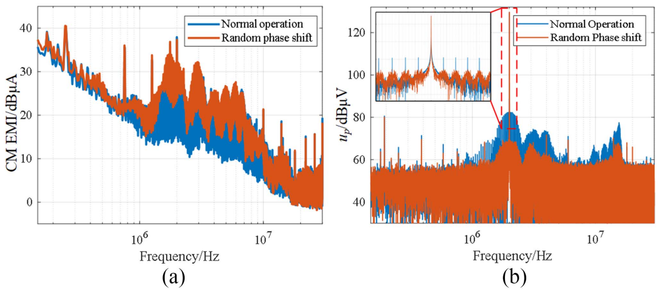

Fig. 46. Measured CM EMI and DM noise under random phase shifting. (a) CM EMI. (b) DM noise.

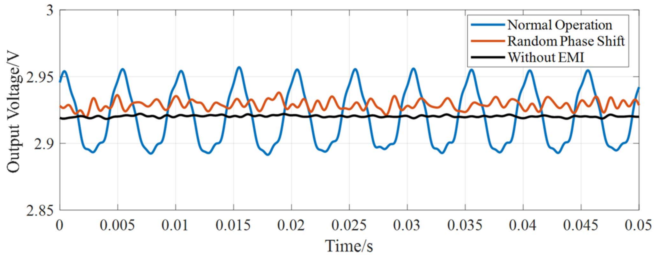

Fig. 47. Tested output signal of the ECS under different modulation.

phase $\Delta\theta$ between the CM voltage pulse edges and the sensor's excitation signal is made to vary randomly, the envelope of the probe voltage will also fluctuate randomly. These random fluctuations can be effectively suppressed by a low-pass filter.

As analyzed in [9], the CM voltage of a two-DOF radial AMB is the average of the bridge voltages of the converter. By adding a random phase shift time $\Delta\alpha$ to all the rising and falling edges of the PWM pulses, the random distribution of CM voltage pulse edges can be achieved, as shown in Fig. 44. Note again that the key factor that matters is the relative phase between CM pulse edge and sinusoidal excitation signal, thus, the phase $\Delta\theta$ can vary randomly within 0–2π as long as the variation range of $\Delta\alpha$ is greater than the period of the excitation signal (500 ns in this article). Therefore, $\Delta\alpha$ is constrained to be between 0 and 500 ns and is set to be uniformly distributed.

The experiment has been done to verify the proposed method. The working condition of the AMB is set the same as mentioned before, and the interference of the ECS is tested with both cable shield and detection surface floated.

The time domain waveforms of probe voltage are shown in Fig. 45. It can be seen that when the system is under normal operation condition, the envelope of the probe voltage fluctuates at a low frequency. After adding a random phase shift time $\Delta\alpha$ to the CM voltage, although the peak value of the interfered probe voltage is not optimized, its envelope no longer changes regularly. The CM EMI and DM noise are shown in Fig. 46. It can be seen that the coupled CM EMI remains almost unchanged because the phase shifting range $\Delta\alpha$ is so small compared with switching period. However, the DM noise exhibits significant attenuation. Thanks to the randomly varied phase $\Delta\theta$, the interference energy concentrated on a certain frequency is dispersed around it, thus greatly reducing the peak of the spectrum. After demodulation and low-pass filtering, the probe voltage yields the output voltage waveform shown in Fig. 47. From Fig. 47, it can be seen that the fluctuations amplitude of the probe output voltage with random phase shift is reduced by more than 70% compared with that with normal operation, demonstrating that the low-pass filter can effectively eliminate the random fluctuated interference. This proves that the proposed method can effectively reduce the impact of CM EMI on the ECS. Additionally, since the phase shift range $\Delta\alpha$ is so small compared with the switching period (50 μs in this article), the output power quality, EMI characteristic and control performance of the AMB controller will be hardly affected, which make this method very flexible and easy to implement to any control algorithm.

D. Comparison of Different Suppression Methods

All the abovementioned EMI effect suppression methods are listed in Table II. Traditional methods include CM chock, grounding and shielding. The CM chock would be good for suppressing both the CM EMI and DM noise, but this is only effective under nongrounded conditions. The grounding of either cable shield or stator frame will provide new low impedance path for CM current, thereby causing the CM chock to be bypassed. Nonideal grounding may be difficult to compensate for the additional interference introduced by this low impedance path, thus, may deteriorate the sensor's output signal.

In contrast, the proposed methods in this article will be better. The symmetrical design of the ECS can endow it with the best EMC, with almost eliminated DM noise and over 95%

TABLE II
COMPARISON OF DIFFERENT SUPPRESSION METHODS

	CM EMI	DM noise	Output signal	Application scope
CM chock	Suppressed	Suppressed	Optimized by 53%	Only for non-grounded conditions.
Grounding and shielding	Provide new low impedance path	Deteriorated	Deteriorated	Depending on the perfection of grounding.
Symmetrical Design	Almost unchanged	Almost eliminated	Optimized over 95%	For preliminary design; need structure change; with best EMC.
Random Phase Shifting	Almost unchanged	Spectrum spread	Optimized over 70%	Only change software; rapid optimization of practical systems

optimization of its output signal. But this method requires the modification of sensor structure, thus, it is only suitable in the preliminary design stage. The random phase shifting method will introduce spectrum spread effect in the DM noise, thus, to suppress its spectral peak and further optimize the output signal by over 70%. This method has the best applicability and can achieve rapid performance optimization without affecting any control framework.

VII. CONCLUSION

The ECS is a crucial part in AMB system to ensure its suspension performance, but it is easily to be affected by CM EMI caused by the drive converter of the AMB. Therefore, this article has conducted in-depth research on this issue. The major conclusions are listed as follows.

1) There are two paths that the CM EMI can couple to the ECS. One is through stray capacitance, which causes high-frequency variations in the frame and rotor voltage, and then conducts to the sensor coil. The other is through radiation, inducing voltage on the sensor cable.
2) The EMI conducting model of the ECS can be built based on measurements and fitting of lumped parameter circuits. The model has been found to accurately reflect the conduction characteristics of EMI in ECS.
3) The high-frequency interference in the probe voltage of ECS mainly originates from DM circulating currents due to asymmetric parameters of the ECS. CM EMI can also cause low-frequency interference in the ECS signal, which is caused by the relative phase shift between the CM voltage and the sensor's sinusoidal excitation signal.
4) Grounding and adding CM inductors to the conditioning circuit may be ineffective in suppressing EMI in the ECS, as the ECS has two interference sources, and grounding provides a low-impedance path for them.
5) Symmetrically designed ECS has good resistance to CM EMI, and random phase shifts in a small range can effectively reduce the low-frequency interference of CM EMI on the ECS.

TABLE III
LIST OF MODEL PARAMETERS

Parameters	Values	Parameters	Values	Parameters	Values
			Probe		
C_{p1}	15.4 pF	C_{p2}	390 pF	R_c	5.55 Ω
ΔR_{cf}	0.23 Ω	ΔR_{cr}	0.37 Ω	R_{pT}	15.25 Ω
L_c	14.0 μH	ΔL_{cf}	2.90 μH	ΔL_{cr}	3.35 μH
L_{pT}	7.63 μH	R_{p2}	14.28 kΩ	R_{p3}	2.02 kΩ
C_{cf}	37.3 pF	C_{cr}	5.58 pF		
			Cable		
R_{10}	57.2 mΩ	R_{11}	0.85 Ω	R_{12}	4.58 Ω
R_{13}	0.14 Ω	L_{10}	0.64 μH	L_{11}	16.9 nH
L_{12}	12.8 nH	L_{13}	30.8 nH	R_2	13.7 mΩ
R_3	10.4 mΩ	L_2	0.52 μH	L_3	0.47 μH
M_{12}	0.53 μH	M_{13}	0.49 μH	M_{23}	0.49 μH
C_{12}	49.0 pF	C_{13}	1.44 pF	C_{23}	184.5 pF
			Conditioning Circuit and Power Supply Module		
R_{s1}	41.5 mΩ	L_{s1}	9.71 nH	C_{s1}	0.45 μF
R_{s2}	41.5 mΩ	L_{s2}	18.77 nH	C_{s2}	0.23 μF
R_{s3}	12.0 mΩ	L_{s3}	5.92 nH	C_{s3}	410.2 μF
R_{s4}	61.9 mΩ	L_{s4}	10.09 nH	C_{s4}	0.22 μF
$C_{s\text{-}cm}$	34.3 pF	R_o	16.0 Ω		
			LISN and CM Inductor		
R_{cmi}	2351 Ω	L_{cmi}	1.29 mH	C_{cmi}	6.87 pF
R_{l1}	0.08 Ω	L_{l1}	5.83 mH	C_{l1}	1.0 μF
R_{l2}	470 Ω				

In short, the work in this article may be helpful for fixing the performance degradation or suspension failure of AMB caused by EMI, and it is beneficial for its reliable operation.

APPENDIX

All the parameters of the high-frequency model of the ECS are listed in Table III.

REFERENCES

[1] H. Wang, Y. Liu, W. Li, and Z. Feng, "Design of ultrastable and high resolution eddy-current displacement sensor system," in *Proc. 40th Annu. Conf. IEEE Ind. Electron. Soc.*, Dallas, TX, USA, 2014, pp. 2333–2339.

[2] Z. Gang, J. Dede, R. Juan, Y. Qingzhen, Z. Xue, and W. Chunlan, "Integrated design and research of active magnetic bearing-sensor," in *Proc. 3rd Int. Conf. Measuring Technol. Mechatron. Automat.*, Shanghai, China, 2011, pp. 433–436.

[3] E. H. Maslen and G. Schweitzer, *Magnetic Bearings: Theory, Design, and Application to Rotating Machinery*. Berlin, Germany: Springer-Verlag, 2009.

[4] D. Pereira and T. G. R. Clarke, "Modeling and design optimization of an eddy current sensor for superficial and subsuperficial crack detection in inconel claddings," *IEEE Sensors J.*, vol. 15, no. 2, pp. 1287–1292, Feb. 2015.

[5] Z. Cao, Y. Huang, F. Peng, and J. Dong, "Driver circuit design for a new eddy current sensor in displacement measurement of active magnetic bearing systems," *IEEE Sensors J.*, vol. 22, no. 17, pp. 16945–16951, Sep. 2022.

[6] B. George, Z. Tan, and S. Nihtianov, "Advances in capacitive, eddy current, and magnetic displacement sensors and corresponding interfaces," *IEEE Trans. Ind. Electron.*, vol. 64, no. 12, pp. 9595–9607, Dec. 2017.

[7] S. Zheng, X. Liu, Y. Zhang, B. Han, Y. Shi, and J. Xie, "Temperature drift compensation for exponential hysteresis characteristics of high-Temperature eddy current displacement sensors," *IEEE Sensors J.*, vol. 19, no. 23, pp. 11041–11049, Dec. 2019.

[8] C. Wang, S. Zheng, B. Han, and Y. Zhang, "Simultaneous temperature drift compensation for eddy current displacement sensors used in magnetically levitated rotor," *IEEE Trans. Instrum. Meas.*, vol. 71, 2022, Art. no. 7504809.

[9] Y. Xie, D. Jiang, F. Hu, and Z. Liu, "Research on common mode EMI and its reduction for active magnetic bearings," *IEEE Trans. Power Electron.*, vol. 38, no. 4, pp. 4246–4250, Apr. 2023.

[10] O. Aiello, P. Crovetti, and F. Fiori, "Investigation on the susceptibility of hall-effect current sensors to EMI," in *Proc. 10th Int. Symp. Electromagn. Compat.*, York, U.K., 2011, pp. 368–372.

[11] Z. Lei, D. Chen, Z. Xiangming, L. JianXuan, and M. Jin, "Research of electromagnetic interference on the eddy current sensor in the inverter-motor driving system," in *Proc. Asia-Pacific Int. Symp. Electromagn. Compat.*, Shenzhen, 2016, pp. 1175–1177.

[12] Z. Lei, L. JianXuan, Z. Xiangming, and M. Jin, "Research of high frequency magnetic field interference on the eddy current sensor," in *Proc. 7th Asia-Pacific Conf. Environ. Electromagnetics*, Hangzhou, China, 2015, pp. 274–277.

[13] J. Yoo, Y.-R. Lee, H. Kim, and S.-K. Sul, "Shielding technique for noise reduction in hall-effect current sensor of voltage source inverter," in *Proc. IEEE Energy Convers. Congr. Expo.*, Detroit, MI, USA, 2022, pp. 1–5.

[14] H. Kim, J. Lee, J. S. Lim, Y. Un Kim, and S.-K. Sul, "Identification and suppression of electromagnetic noise of variable reluctance resolver for hybrid electric vehicle," in *Proc. IEEE Transp. Electrific. Conf. Expo*, Anaheim, CA, USA, 2022, pp. 13–17.

[15] F. L. Fiori and P. S. Crovetti, "Prediction of high-power EMI effects in CMOS operational amplifiers," *IEEE Trans. Electromagn. Compat.*, vol. 48, no. 1, pp. 153–160, Feb. 2006.

[16] M. V. Quitadamo and F. Fiori, "A SPICE model of operational amplifiers for electromagnetic susceptibility analysis," *IEEE Trans. Electromagn. Compat.*, vol. 64, no. 2, pp. 418–428, Apr. 2022.

[17] C. Sui, L. Ren, X. Gao, J. Pan, J. L. Drewniak, and D. G. Beetner, "Predicting statistical characteristics of jitter due to simultaneous switching noise," *IEEE Trans. Electromagn. Compat.*, vol. 58, no. 1, pp. 249–256, Feb. 2016, doi: 10.1109/TEMC.2015.2474124.

[18] H. Chen, T. Wang, S. Ye, and T. Zhou, "Modeling and suppression of electromagnetic interference noise on motor resolver of electric vehicle," *IEEE Trans. Electromagn. Compat.*, vol. 63, no. 3, pp. 720–729, Jun. 2021.

[19] J. Yu, R. Burgos, and D. Boroyevich, "EMI study on control implementation in PEBB-based converter," in *Proc. IEEE 19th Workshop Control Model. Power Electron.*, Padua, Italy, 2018, pp. 1–5.

[20] O. Aiello and F. Fiori, "A new current sensor based on MagFET highly immune to EMI," in *Proc. Int. Conf. Electromagnetics Adv. Appl.*, Turin, Italy, 2009, pp. 784–787.

[21] O. Aiello and F. Fiori, "A new current sensor based on the Miller effect highly immune to EMI," in *Proc. Asia-Pacific Symp. Electromagn. Compat.*, Singapore, 2012, pp. 69–72.

[22] C. Pan, S. Ren, F. Yang, C. Shi, H. Zuo, and Z. Feng, "Suppression of low-frequency magnetic interference on eddy current displacement sensor with nanometer resolution," in *Proc. Int. Conf. Sens., Meas. Data Analytics Era Artif. Intell.*, Xi'an, China, 2020, pp. 11–16.

[23] M. R. Nabavi and S. Nihtianov, "Eddy-current sensor interface for advanced industrial applications," *IEEE Trans. Ind. Electron.*, vol. 58, no. 9, pp. 4414–4423, Sep. 2011.

[24] A. S. Reddy, P. K. Agarwal, and S. Chand, "Design of compact active magnetic bearing with higher load carrying capacity," in *Proc. Students Conf. Eng. Syst.*, Allahabad, India, 2012, pp. 1–5.

[25] H.-J. Hu, K. Liu, H. Wang, and J.-B. Wei, "A wide bandwidth GaN switching power amplifier of active magnetic bearing for a flywheel energy storage system," *IEEE Trans. Power Electron.*, vol. 38, no. 2, pp. 2589–2605, Feb. 2023.

[26] B. Zhang, S. Wang, Y. Lai, and Y. Yang, "Modeling and prediction of low-frequency radiated EMI for a SiC motor drive system," *IEEE Trans. Ind. Electron.*, vol. 71, no. 9, pp. 10210–10220, Sep. 2024.

[27] A. F. Moreira, T. A. Lipo, G. Venkataramanan, and S. Bernet, "High frequency modeling for cable and induction motor overvoltage studies in long cable drives," in *Proc. Conf. Rec. IEEE Ind. Appl. Conf., 36th IAS Annu. Meeting*, Chicago, IL, USA, 2001, vol. 3, pp. 1787–1794.

[28] L. Wang, C. Ngai-Man Ho, F. Canales, and J. Jatskevich, "High-frequency modeling of the long-cable-fed induction motor drive system using TLM approach for predicting overvoltage transients," *IEEE Trans. Power Electron.*, vol. 25, no. 10, pp. 2653–2664, Oct. 2010.

[29] A. Ganjavi, F. Zare, D. Kumar, A. M. Abbosh, K. S. Bialkowski, and P. Davari, "Mathematical model of common-mode sources in long-cable-fed adjustable speed drives," *IEEE Trans. Ind. Appl.*, vol. 58, no. 2, pp. 2013–2028, Mar./Apr. 2022.

[30] I. Stevanović, B. Wunsch, G. L. Madonna, and S. Skibin, "High-frequency behavioral multiconductor cable modeling for EMI simulations in power electronics," *IEEE Trans. Ind. Inform.*, vol. 10, no. 2, pp. 1392–1400, May 2014.

[31] H. Bishnoi, A. C. Baisden, P. Mattavelli, and D. Boroyevich, "Analysis of EMI terminal modeling of switched power converters," *IEEE Trans. Power Electron.*, vol. 27, no. 9, pp. 3924–3933, Sep. 2012.

[32] M. Depenbrock, "Quantities of a multiterminal circuit determined on the basis of Kirchhoff's laws," *Eur. Trans. Elect. Power*, vol. 8, no. 4, pp. 249–257, 2010.

[33] Q. Li, B. Xie, Y. Zhang, J. Ma, and C. Yuan, "A general analytical model of single-layer common-mode chokes," *IEEE Trans. Power Electron.*, vol. 39, no. 6, pp. 6591–6596, Jun. 2024.

[34] B. Xie, Q. Li, Y. Zhang, and C. Yuan, "High-frequency electromagnetic behavior, impedance modeling, and enhancement of low-permeability powder cores," *IEEE Trans. Power Electron.*, vol. 40, no. 2, pp. 3336–3356, Feb. 2025.

Yuanhao Xie (Graduate Student Member, IEEE) was born in Chongqing, China, in 1997. He received the B.S. degree in electrical engineering from Chongqing University, Chongqing, China, in 2019. He is currently working toward the Ph.D. degree in electrical engineering with Huazhong University of Science and Technology, Wuhan, China.

His current research interests include power hardware-in-the-loop system, electromagnetic interference, and active magnetic bearings.

Dong Jiang (Senior Member, IEEE) received the B.S. and M.S. degrees in electrical engineering from Tsinghua University, Beijing, China, in 2005 and 2007, respectively, and the Ph.D. degree in power electronics and motor drives from the University of Tennessee, Knoxville, TN, USA, in 2011.

He was with the United Technologies Research Center, East Hartford, CT, USA, as a Senior Research Scientist/Engineer, from 2012 to 2015. He has been with the Huazhong University of Science and Technology, Wuhan, China, as a Professor, since July 2015. He has authored and coauthored more than 200 IEEE journal and conference papers and more than 80 granted patents in the area of his research interests, which include power electronics and motor drives.

Dr. Jiang is an Associate Editor for IEEE TRANSACTIONS ON INDUSTRY APPLICATIONS. He was the recipient of several best paper awards in IEEE conferences. He is the chair of IEEE Power Electronics Society (IEEE PELS) Wuhan Chapter and Regional Distinguished Lecturer of IEEE PELS.

Jianfu Ding (Graduate Student Member, IEEE) was born in Liaoning, China, in 1998. He received the B.S. degree in electrical engineering and the M.S. degree in new energy science and engineering in 2020 and 2023, respectively, from Huazhong University of Science and Technology, Wuhan, China, where he is currently working toward the Ph.D. degree in electrical engineering.

His current research interests include multilevel converter topology, control strategy, and modulation method for active magnetic bearings.

Zicheng Liu (Senior Member, IEEE) was born in Shandong, China, in 1989. He received the B.S. degree in hydropower engineering from Huazhong University of Science and Technology (HUST), Wuhan, China, in 2011, and the Ph.D. degree in electrical engineering from Tsinghua University, Beijing, China, in 2016.

From 2014 to 2015, he was a Visiting Student with Purdue University, West Lafayette, IN, USA. From 2016 to 2018, he was a Postdoc Researcher with Beijing Jiaotong University, Beijing, China. He is currently an Associate Professor with HUST. His research interests include multiphase motor control systems and transportation electrification.